

## Numerical Prediction of Radiation and Air Preheating Effects on the Soot Formation in a Confined Laminar Co-Flow Diffusion Flame

Achin Kumar Chowdhuri<sup>1</sup>, Somnath Chakrabarti<sup>2</sup> and Bijan Kumar Mandal<sup>3,\*</sup>

Department of Mechanical Engineering, Bengal Engineering and Science University, Shibpur,  
Howrah, West Bengal, 711103, India  
E-mail: <sup>1</sup>achinkumar\_becs@rediffmail.com  
E-mail: <sup>2</sup>somnathbec@rediffmail.com  
E-mail: <sup>3</sup>[bkm375@yahoo.co.in](mailto:bkm375@yahoo.co.in)

Received 07 April 2014, Accepted 22 September 2014

### Abstract

A numerical model has been developed for thorough investigation of the radiation and air-preheating effect on the sooting behavior of a diffusion flame. An explicit finite difference scheme has been adopted for the solution of different conservation equations for reacting flows along with the soot conservation equations. A variable size adaptive grid system has been considered using hyperbolic distribution to capture the sharp gradients of the field variables. Temperature distribution pattern does not change when radiation effect is considered, but peak temperature is lowered due to radiative heat loss. On the other hand, air-preheating not only increases the peak temperature, but also changes the distribution pattern significantly. Radiation decreases the soot volume fraction and soot number density to a large extent both for non-preheated and preheated case. Soot diameter is not much affected due to radiation, but it increases with preheating of air.

**Keywords:** Diffusion flame; finite difference; soot; radiation; preheating; temperature; number density.

### 1. Introduction

Soot produced in a flame has both beneficial and detrimental effects. The properties of soot reaction in flames represent unsolved combustion problem having significant relevance to the society. In applications like furnaces, the radiation heat transfer associated with soot particles provides a more uniformly heated environment. But the detrimental effects of the soot particles are enormous compared with its beneficial effects. Soot particles in any combustion exhaust is viewed as environmental pollution and it is observed that soot particulate emitted as a pollutant from combustion processes causes more deaths than any other combustion generated pollutant. The understanding of the complex processes of formation of soot particles in the high temperature regions of the flames is limited and extensive research works are needed for the advancement of practical combustor designs. Research interest has thus been increased recently devoting to the numerical modeling of axi-symmetric co-flow diffusion flames because these flames allow relatively simple calculations of detailed gas-phase chemistry coupled with a simplified soot formation model and different treatments of radiation heat transfer. Some recent works on soot formation and soot modeling have been presented in the next part.

Ku *et al.* [1] studied numerically and experimentally the soot formation and radiative heat transfer in acetylene-air and ethylene-air jet diffusion flames under normal gravity and microgravity conditions. McEnally *et al.* [2] observed that gas cooling effects due to radiative loss significantly change the predicted temperature. Syed *et al.* [3] proposed a two equations soot model for laminar diffusion flames with different fuels. Moss *et al.* [4] developed a simplified model of soot formation, based on laminar flamelet approach with

a view to subsequent turbulent flame prediction and also inclusion of radiation. Said *et al.* [5] proposed a simple two-equation model for soot formation and oxidation. The radiation losses had been found to be important and it was necessary to include them in the model. Sivathanu and Gore [6] numerically solved the transport equations for mass, momentum, mixture fraction, enthalpy including gas band radiation to find soot number density and soot mass fraction for a methane-air laminar diffusion flame using simplified soot kinetics. Smooke *et al.* [7] developed a detailed soot growth model for an axisymmetric, laminar, coflow diffusion flame by coupling the equations of particle production to the flow and gaseous species conservation equations.

Liu *et al.* [8] conducted a computational study of soot formation in an axi-symmetric ethylene-air coflow jet diffusion flame at atmospheric pressure to investigate the effect of radiative heat transfer from the gases and soot on the flame structure and soot field. Guo *et al.* [9] studied numerically, the effect of preheating on soot formation for an axisymmetric, laminar co flow diffusion ethylene-air flame. They claimed that the flame preheating effect had a significant influence on the prediction of soot formation process. Smooke *et al.* [10] studied laminar, sooting, coflow diffusion flames experimentally and computationally and observed that the impact of radiative power loss on temperature had a significant effect on soot formation. Kamal [11] carried out a numerical study to address the sooting characteristics of normal and inverse diffusion flames on the basis of single step kinetics with a laminar flow assumption and non-unity Lewis number. Saji *et al.* [12] studied numerically and experimentally a laminar ethylene-air ambient air co-flowing jet diffusion flame. They used a two-equation transport model for soot growth and

oxidation processes and formed the radiative heat transfer model using the PI approximation.

The mechanism of soot formation is not yet fully understood, but, it is understood that radiation and air-preheating will change the scenario significantly. Although there are several studies on the effect of radiation heat loss on the sooting behavior of diffusion flames, the combined effect of air-preheating and radiation is not addressed properly in the literature. This motivates the authors to get a close picture about the sooting phenomena in a coflow laminar methane-air diffusion flame by using a simple chemical kinetics and considering the radiation and air-preheating effect. For this purpose, a numerical model for reacting flows has been developed. The model is completed by inserting an optically thin radiation model and a semi-empirical soot model. The predictions from the in-house code developed for this purpose are presented in terms of temperature distribution and different soot parameters.

## 2. Mathematical Model

The physical model considered here is a coflow burner consisting of two concentric vertical tubes. Fuel (methane) is admitted as a central jet through the inner tube and air (oxidizer) as a co-flowing annular jet through the outer tube. The inner fuel tube diameter is 12.7 mm and the outer tube diameter is 50.4 mm. The dimensions are taken as same as that of the earlier experimental work of Mitchell *et al.* [13] and the numerical work of Smooke *et al.* [14]. The flow is assumed to be laminar, and the geometry is confined and axisymmetric. The schematic of the combustion system is shown in Figure 1(a) and Figure 1(b) shows the grid arrangement for the computational work on one side of the axis. The numerical solution is obtained solving gas phase conservation equations along with suitable equations for soot and radiation modeling. As the geometry of the model is symmetrical about the central axis, a two dimensional (2-D) simulation has been carried out. In cylindrical co-ordinates ( $r, \theta, z$ ), the parameters will not vary along  $\theta$  direction.

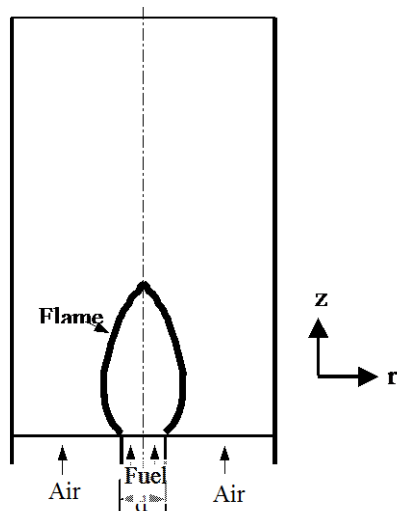


Figure 1(a). Schematic diagram of the burner and the flame geometry.

### 2.1 Governing Equations

The conservation equations considered here for mass, momentum, species and energy in cylindrical co-ordinates for an axisymmetric system can be written as:

Mass:

$$\frac{\partial \rho}{\partial t} + \frac{1}{r} \frac{\partial}{\partial r} (r \rho v_r) + \frac{\partial}{\partial z} (\rho v_z) = 0 \quad (1)$$

Radial Momentum:

$$\begin{aligned} & \frac{\partial}{\partial t} (\rho v_r) + \frac{1}{r} \frac{\partial}{\partial r} (r \rho v_r^2) + \frac{\partial}{\partial z} (\rho v_r v_z) \\ &= -\frac{\partial p}{\partial r} + \frac{2}{r} \frac{\partial}{\partial r} \left( r \mu \frac{\partial v_r}{\partial r} \right) - \frac{2}{r} \mu \frac{v_r}{r^2} + \frac{\partial}{\partial z} \left\{ \mu \left( \frac{\partial v_z}{\partial r} + \frac{\partial v_r}{\partial z} \right) \right\} \\ & - \frac{2}{3} \frac{\partial}{\partial r} \left( \mu \left( \frac{\partial v_r}{\partial r} + \frac{v_r}{r} + \frac{\partial v_z}{\partial z} \right) \right) \end{aligned} \quad (2)$$

Axial Momentum:

$$\begin{aligned} & \frac{\partial}{\partial t} (\rho v_z) + \frac{1}{r} \frac{\partial}{\partial r} (r \rho v_r v_z) + \frac{\partial}{\partial z} (\rho v_z^2) \\ &= -\frac{\partial p}{\partial z} + \frac{1}{r} \frac{\partial}{\partial r} \left\{ r \mu \left( \frac{\partial v_z}{\partial r} + \frac{\partial v_r}{\partial z} \right) \right\} + 2 \frac{\partial}{\partial z} \left( \mu \frac{\partial v_z}{\partial z} \right) \\ & - \frac{2}{3} \frac{\partial}{\partial z} \left\{ \mu \left( \frac{\partial v_r}{\partial r} + \frac{v_r}{r} + \frac{\partial v_z}{\partial z} \right) \right\} + \rho g \end{aligned} \quad (3)$$

Species:

$$\begin{aligned} & \frac{\partial}{\partial t} (\rho C_j) + \frac{1}{r} \frac{\partial}{\partial r} (r \rho v_r C_j) + \frac{\partial}{\partial z} (\rho v_z C_j) \\ &= \frac{1}{r} \frac{\partial}{\partial r} \left( r \rho D_{jm} \frac{\partial C_j}{\partial r} \right) + \frac{\partial}{\partial z} \left( \rho D_{jm} \frac{\partial C_j}{\partial z} \right) + \dot{S}_{cj} \end{aligned} \quad (4)$$

$j = 1, 2, 3, 4, 5$

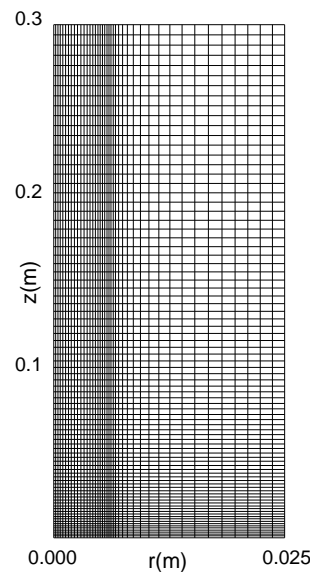


Figure 1(b). Grid structure.

Energy:

$$\begin{aligned} \frac{\partial}{\partial t}(\rho h) + \frac{1}{r} \frac{\partial}{\partial r}(r \rho v_r h) + \frac{\partial}{\partial z}(\rho v_z h) &= \frac{1}{r} \frac{\partial}{\partial r} \left( r \frac{\lambda}{c_p} \frac{\partial h}{\partial r} \right) \\ &+ \frac{\partial}{\partial z} \left( \frac{\lambda}{c_p} \frac{\partial h}{\partial z} \right) - \frac{1}{r} \frac{\partial}{\partial r} (r q_{R_r}'' ) - \frac{\partial}{\partial z} (q_{R_z}'' ) \\ &+ \frac{1}{r} \frac{\partial}{\partial r} \left[ r \frac{\lambda}{c_p} \sum_{j=1}^n h_j (Le_j^{-1} - 1) \frac{\partial C_j}{\partial r} \right] \\ &+ \frac{\partial}{\partial z} \left[ \frac{\lambda}{c_p} \sum_{j=1}^n h_j (Le_j^{-1} - 1) \frac{\partial C_j}{\partial z} \right] \end{aligned} \quad (5)$$

The combustion reaction of methane and air is assumed to proceed through simplified two-step global reaction chemistry. The conservation equation for chemical species is solved for five gaseous species, viz. CH<sub>4</sub>, O<sub>2</sub>, CO<sub>2</sub>, CO and H<sub>2</sub>O. Specific heat of the mixture is then calculated considering an ideal gas mixture. The temperature of the gas mixture is implicitly calculated from enthalpy by using Newton-Raphson method. The transport of momentum, energy and species mass in the calculation of a reacting flow involve the transport coefficients like viscosity ( $\mu$ ), thermal conductivity ( $\lambda$ ) and mass diffusivity ( $D_{jm}$ ) for the solution. The variations of these properties with temperature have been taken care of using suitable polynomials and correlations.

## 2.2 Radiation Model

Through a heat source term, radiation enters the energy conservation equation Eq. (5) which is expressed as the divergence of the radiative heat flux. This is found by solving the radiative transport equation using the appropriate model as done by Datta and Saha [15]. Using an optically thin radiation model, the radiative source term is evaluated as

$$\nabla \cdot q_{R_r}'' = 4\sigma k (T^4 - T_b^4) \quad (6)$$

In the above equation, T and T<sub>b</sub> are local temperature and background temperature respectively. However, background temperature is considered to be negligible in this work.  $\sigma$  is the Stefan-Boltzmann constant and absorption coefficient k is obtained from

$$k = k_{\text{gas}} + k_{\text{soot}} \quad (7)$$

where  $k_{\text{gas}}$  is the gas phase contribution of absorption coefficient and  $k_{\text{soot}}$  is the soot contribution of absorption coefficient. The coefficient,  $k_{\text{gas}}$  is obtained from

$$\begin{aligned} k_{\text{gas}} &= Y_{\text{CO}_2} k_{\text{CO}_2}(T) + Y_{\text{H}_2\text{O}} k_{\text{H}_2\text{O}}(T) + \\ &Y_{\text{CO}} k_{\text{CO}}(T) + Y_{\text{CH}_4} k_{\text{CH}_4}(T) \end{aligned} \quad (8)$$

where  $Y_i$  and  $k_i$  indicate the mole fraction and Planck mean absorption coefficient, respectively, of the species i.  $k_{\text{soot}}$  is obtained from

$$k_{\text{soot}} = 1862 f_v T \quad (9)$$

where  $f_v$  and T represent the local values of soot volume fraction and temperature, respectively. Planck mean absorption coefficients of species in Eq. (8) are taken from Barlow *et al.* [16].

## 2.3. Soot Formation Model

The soot formation is based on the work of Syed *et al.* [3] and Moss *et al.* [4]. The soot volume fraction ( $f_v$ ) and number density ( $n$ ) are considered to be the important variables. Nucleation, surface growth, coagulation and oxidation effects are taken into account in the formation of the model equations. The specific rate of soot oxidation ( $\omega_{\text{OX}}$ ) has been calculated using the model of Lee *et al.* [17]. The conservation equations are formed for soot mass concentration ( $\rho_s f_v$ ) and number density (as  $n/N_o$ ) and the respective generation terms for the conservation equations are as follows:

$$\begin{aligned} \frac{d}{dt}(\rho_s f_v) &= \gamma (\rho_s f_v)^{2/3} n^{1/3} \\ &+ \delta - \left( \frac{36\pi}{\rho_s^2} \right)^{1/3} (n \rho_s^2 f_v^2)^{1/3} \omega_{\text{OX}} \end{aligned} \quad (10)$$

$$\frac{d}{dt} \left( \frac{n}{N_o} \right) = \alpha - \beta \left( \frac{n}{N_o} \right)^2 \quad (11)$$

where

$$\alpha = C_\alpha \rho^2 T^{0.5} X_c \exp\left(-\frac{T_\alpha}{T}\right)$$

$$\beta = C_\beta T^{0.5}$$

$$\gamma = C_\gamma \rho T^{0.5} X_c \exp\left(-\frac{T_\gamma}{T}\right)$$

$$\delta = C_\delta \alpha$$

In the above equations and expressions,  $N_o$  is Avogadro number ( $6 \times 10^{26}$ ),  $\rho_s$  is the soot particulate density ( $=1800 \text{ kg/m}^3$ ),  $X_c$  is the mole fraction of the parent fuel species.  $T_\alpha$  and  $T_\gamma$  are activation temperatures for nucleation and growth, respectively,  $C_\alpha$ ,  $C_\beta$ ,  $C_\gamma$ ,  $C_\delta$  are model constants and,  $\rho$  and T are the local mixture density and temperature, respectively. The model constants and activation temperatures are taken from Syed *et al.* [3] for methane fuel. The general conservation equations for different soot variables can be expressed as

$$\begin{aligned} \frac{\partial \varphi}{\partial t} + \frac{1}{r} \frac{\partial}{\partial r} (r v_r \varphi) + \frac{\partial}{\partial z} (\rho v_z \varphi) &= \\ \frac{1}{r} \frac{\partial}{\partial r} (r V_{t_r} \varphi) + \frac{\partial}{\partial z} (V_{t_z} \varphi) + \dot{S}_\varphi \end{aligned} \quad (12)$$

The above equation is applicable both for the soot mass concentration ( $\rho_s f_v$ ) and number density ( $n/N_o$ ) and

accordingly  $\phi$  in Eq.(12), will assume the respective variable value. The thermophoretic velocity vector is calculated following Santoro *et al.* [18].

#### 2.4. Boundary Conditions

Boundary conditions at the inlet have been given separately for the fuel stream at the central jet and the air stream at the annular co-flow. The streams are considered to enter the computational domain as plug flow, with velocities calculated from their respective flow rate. The temperatures of fuel and air have been specified. In conformation with the conditions used by Mitchell *et al.* [13] and Smooke *et al.* [14], the fuel flow rate is taken as  $3.71 \times 10^{-6}$  kg/s and the air flow rate is taken as  $2.214 \times 10^{-4}$  kg/s. No soot is considered to enter with the flow through the inlet plane. Considering the length of the computational domain to be 0.3 m, the fully developed boundary conditions for the variables are considered at the outlet. In case of reverse flow at the outlet plane, which occurs in the case of buoyant flame, the stream coming in from the outside is considered to be ambient air. Axi-symmetric condition is considered at the central axis, while at the wall a no-slip, adiabatic and impermeable boundary conditions are adopted. Boundary conditions for soot formation are given separately. The thermophoretic velocities required for soot calculations are considered to be zero at the boundaries.

#### 2.5. Numerical Scheme

The gas phase conservation equations of mass, momentum and energy and species along with the conservation equations of soot mass concentration and soot number density are solved simultaneously, with their appropriate boundary conditions, using explicit finite difference method. The solution yields velocity, temperature and species concentration, soot mass concentration and soot number density at each grid point of the computational domain. The numerical scheme adopted for this simulation is based on a straight-forward algorithm called SOLA (Solution Algorithm) originally developed by Hirt and Cook [19] and modified by Datta [20] for reacting flows. The algorithm is based on primitive variables and the variables are defined following a staggered grid arrangement. The axial and radial components of velocity are defined at the scalar cell faces while the relevant scalar properties (pressure, temperature, species concentration and soot variables), the fluid properties (density, viscosity and specific heat) and the source terms (volumetric rates of heat generation and species, soot) are defined at the centers of the cells. The solution is explicitly advanced in time till a steady state convergence is achieved. The solution is considered to be convergent when the temporal derivatives of temperature and velocity at all grids become less than an assigned small value.

The transient transport equations are discretized using explicit finite differencing technique. The diffusion terms are discretized by a central differencing scheme, whereas the advection terms are discretized by a hybrid differencing schemes as described by Patankar [21]. In the latter scheme, the advection terms are discretized in central differencing mode when the cell Peclet number lies in the range  $-2 \leq Pe \leq 2$ . When the cell Peclet number becomes outside this range, the discretization scheme reduces to upwind or donor-cell differencing method in which the diffusion terms of the discretized transport equations are set to zero. The

fluid properties like density, specific heat and viscosity are calculated at the cell faces by linear interpolation between the corresponding property values at the adjacent cell centers. This is meant to maintain the conservativeness of the convection and diffusion flux components respectively across the computational domain. The source terms are considered to be constant throughout the volume of each cell.

A variable size adaptive grid system is considered using hyperbolic distribution to capture the sharp gradients of the field variables. It is expected that the fuel and air streams, after issuing as the respective jets, diffuse into each other to form a flammable mixture close to the burner tip. The burner-stabilized flame should, therefore, stay very close to the burner and a high temperature gradient will be present in the axial direction. Therefore, in the axial direction, clustering of cells is done near the inlet. In the radial direction, clustering is done at the proximities of the wall and the line of symmetry to capture the variation there. Moreover, at the fuel-oxygen interface near the inlet the cells are kept fine radially. The diffusion of reactant species from both sides into the flame and the transport of heat from flame zone cause a high radial gradient at such interface, which can only be captured by keeping the grid sizes small. However, the variations in the size of the grids are ensured to be gradual. The difference in the linear dimensions of two adjacent cells is kept below 15%. An extensive grid independence test is carried out by several variations of the number of grids in either direction and a numerical mesh with  $85 \times 41$  grid nodes is finally adopted.

#### 2.6. Solution Procedure

The different conservation equations, namely, the momentum, energy, species concentration, soot mass concentration and number density conservation equations are solved for the time,  $t_n + \delta t$ , by explicit method, using current values of the field variables like pressure, velocity, species concentration, temperature distribution, soot mass concentration and soot number distributions over the computed at the  $n^{\text{th}}$  time step,  $t_n$ . Calculated values of the different fluid properties at the  $n^{\text{th}}$  time step are also used for the next time step as well. The resulting velocity field for the time-step,  $t_n + \delta t$ , generally does not satisfy the continuity equation. This is obviously due to the incorrect pressure field assumption in the momentum equation. The required pressure correction could be done only through the continuity equation, but it does not includes any pressure term. So it is achieved by imposing the constrain of zero mass divergence iteratively. For each cell, the mass divergence ( $D_{i,j}$ ) is computed using the most recently corrected velocities. The pressure correction,  $\delta p_{i,j}$ , required to set the absolute values of  $D_{ij}$  below a small pre-assigned number (0.001 in this work) is calculated as

$$\delta p_{i,j} = \frac{\beta \cdot D_{i,j}}{\delta t \left\{ \frac{1}{r_j \delta r_j} \left( \frac{r_j}{\delta r_j} + \frac{r_{j-1}}{\delta r_{j-1}} \right) + \frac{1}{\delta z_i} \left( \frac{1}{\delta z_i} + \frac{1}{\delta z_{i-1}} \right) \right\}} \quad (13)$$

where,  $\beta$  is an over-relaxation parameter used to accelerate convergence.

The change in pressure within a cell corrects the associated velocity components at the scalar cell faces as follows

$$v_r(i,j) = \tilde{v}_r(i,j) + \frac{1}{\rho_n} \frac{\delta t \cdot \delta p_{i,j}}{\delta r_j} \quad (14)$$

$$v_r(i,j-1) = \tilde{v}_r(i,j) - \frac{1}{\rho_s} \frac{\delta t \cdot \delta p_{i,j}}{\delta r_{j-1}} \quad (15)$$

$$v_z(i,j) = \tilde{v}_z(i,j) + \frac{1}{\rho_e} \frac{\delta t \cdot \delta p_{i,j}}{\delta z_i} \quad (16)$$

$$v_z(i-1,j) = \tilde{v}_z(i,j) - \frac{1}{\rho_w} \frac{\delta t \cdot \delta p_{i,j}}{\delta z_{i-1}} \quad (17)$$

where,  $\rho_e$ ,  $\rho_w$ ,  $\rho_n$  and  $\rho_s$  denote the fluid densities at the right, left, top and bottom faces respectively, of the scalar cell (Fig. 2). The cell pressure is also corrected accordingly.

Once the continuity equation is satisfied at the time-step,  $t_n + \delta t$ , and a correct pressure field is obtained, other conservation equations are solved to calculate the field variables at that time-step. The temperature of the gas mixture is then implicitly calculated from enthalpy and mass fraction values using Newton-Raphson method. Density is then computed from the ideal gas relationship using the values of species concentration and temperature at the time-step,  $t_n + \delta t$ , and the corrected absolute pressure field.

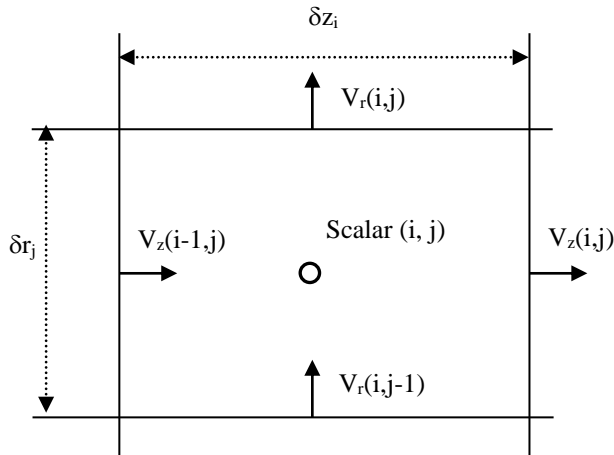


Figure 2. Scalar cell with velocities at the cell faces.

## 2.7. Stability Criteria

The choice of the incremental time-step has to be done very carefully as it is directly related to the stability of the explicit scheme. The restrictions suggested by Hirt *et al.* [22] are used here. The first criteria demands that pure advection should not convey a fluid element past a cell in one time increment as the difference equations consider fluxes only between adjacent cells. Hence the time increment should satisfy the following inequality.

$$\delta t_1 < \min \left\{ \frac{\delta r}{|v_r|}, \frac{\delta z}{|v_z|} \right\} \quad (18)$$

The second constrain puts a restriction on the grid Fourier number, such that the fluxes should not diffuse more than one cell length in one time increment. This restriction on the incremental time is imposed through the following condition.

$$\delta t_2 < \frac{0.5}{\max\{v, \alpha, D\}} \times \frac{\delta r^2 \delta z^2}{(\delta r^2 + \delta z^2)} \quad (19)$$

Incremental time-step using both the criteria is calculated for all the cells in the entire domain. Finally, the incremental time-step is chosen considering both the criteria together and it is given by

$$\delta t = \min \{ \delta t_1, \delta t_2 \} \quad (20)$$

However, during the computation, the actual values of  $\delta t$  are suitably scaled down in order to ensure the convergence of the problem.

## 2.8. Ignition

The ignition of the fuel-air mixture in the combustion chamber is simulated by raising the temperature of the mixture within a few cells, to 1000 K, near the fuel-air interface (slightly above the burner tip) and maintaining it there till the local temperature of the flammable mixture is raised beyond the ignition temperature due to reaction. This is achieved by adding a heat source of suitable value in such a way that the combustion sustains and also remains within the control. The location of ignition (i.e., heat source addition points) is chosen considering the fact that the concentration ratio of the fuel and air in the corresponding cells remains within the flammability limit.

## 3. Results and Discussion

The simulation has been carried out for four flame conditions with consideration of radiation and non-radiation for non-preheated as well as preheated air. The operating conditions for the flames are listed in table 1. The two terms corresponding to radiative heat fluxes in  $z$  and  $r$  directions in the energy equation are dropped to get the results for the case of without radiation. Flame I can be considered as the base flame for the comparison.

### 3.1. Validation of the Code

The predictions from the present simulation have been compared with the experimental results of Mitchel *et al.* [13]. The validation is carried out for non-preheated air with inlet temperature of 300 K and fuel inlet temperature of 300 K considering radiation effect and also without considering radiation effect. Figure 3 (a) and 3 (b) show the temperature distributions at axial positions of 1.2 cm and 5.0 cm above the burner tip. At 1.2 cm axial position it is matching although the peak temperature is slightly over predicted at the fuel-air interface. Temperature is under predicted near the axis and over predicted away from the axis to certain radial distance from the axis. But in both

Table 1. Operating Conditions for Different Flames Investigated.

Parameters	Flame I	Flame II	Flame III	Flame IV
Pressure (N/m <sup>2</sup> )	1.0132×10 <sup>5</sup>	1.0132×10 <sup>5</sup>	1.0132×10 <sup>5</sup>	1.0132×10 <sup>5</sup>
Fuel flow rate (kg/s)	3.71×10 <sup>-6</sup>	3.71×10 <sup>-6</sup>	3.71×10 <sup>-6</sup>	3.71×10 <sup>-6</sup>
Air flow rate (kg/s)	2.214×10 <sup>-4</sup>	2.214×10 <sup>-4</sup>	2.214×10 <sup>-4</sup>	2.214×10 <sup>-4</sup>
Fuel inlet temperature (K)	300 K	300 K	300 K	300 K
Air inlet temperature (K)	300	300 K	400 K	400 K
Fuel inlet velocity (m/s)	0.0450	0.0450	0.0450	0.0450
Air inlet velocity (m/s)	0.0988	0.0988	0.1335	0.1335
Radiation effect	Not considered	Considered	Not considered	Considered
Air preheating	No	No	Yes	Yes

cases, deviation is not much from the experimental work of Mitchel *et al.* [13].

The soot code is validated with the previous work of Smooke *et al.* [10] at two non-dimensional axial heights of 0.50 and 0.70 for non-preheated air. The radial distributions of soot volume fraction at the above two heights have been shown in figures 4(a) and 4(b) respectively. The results from the experimental and numerical works of Smooke *et al.* [10] have also been plotted on the same figures for comparison. It can be observed from the figures that there is a difference in the numerical values between the experimental values of Smooke *et al.* [10] and the present predictions. It is also observed that the present simulation correctly predicts the trend and location of peak values particularly at non-dimensional axial heights of 0.70. It can also be seen that the present prediction is sometimes better than the numerical results of Smooke *et al.* [10]. When radiation is neglected the predicted values are slightly higher as expected. In all the numerical cases, the values are under predicted. The relatively simple kinetics considered for this work here may not capture all the mode of soot formation process due to its limitation in number of intermediate species and the number of reaction steps.

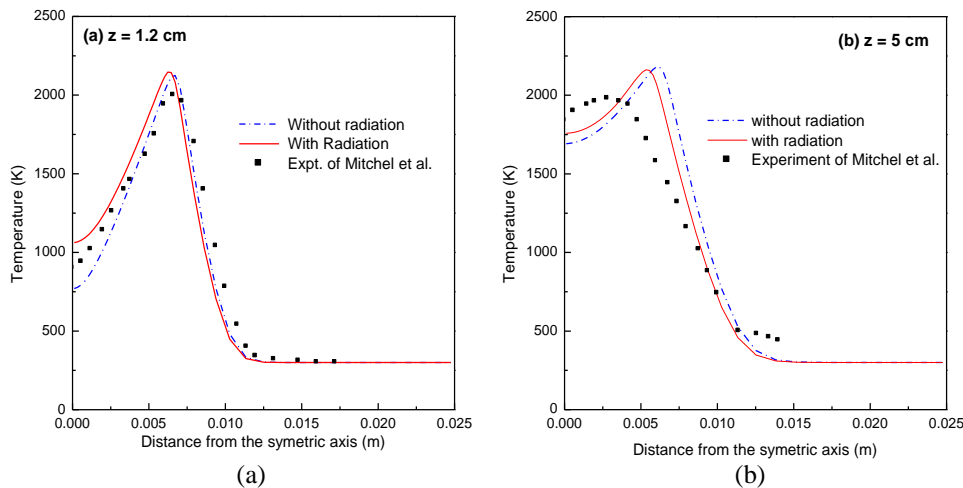


Figure 3. Comparison of the predicted radial distribution of temperature with the experimental data of Mitchell *et al.* [13] at two axial heights of (a)  $z = 1.2$  cm and (b)  $z = 5.0$  cm above the burner.

### 3.2. Temperature Distribution

Temperature plays a very important role in the soot formation process in jet diffusion flames. The isotherm patterns for different flames have been shown in figures 5 (a) to 5 (d). A close look into the temperature distribution patterns reveals that the basic pattern at the same temperature of inlet air (300 K for non-preheated and 400 K for preheated air) does not change, but temperature decreases to some extent when radiation effect is considered. If radiation is not considered, then a contour of

even 2100 K is clearly seen in Fig. 5 (a). But when radiation exchange is taken into consideration, the highest temperature contour that can be distinctly observed in the computation domain is of 2000 K as shown in Fig.5 (b). The radiation effect is more prominent when preheated air is used as observed from Fig. 5 (c) and Fig. 5 (d). Another important feature that can be observed from the temperature contours is that isotherms are almost vertical in case of non-preheated air whether radiation effect is taken into consideration or not. The temperatures near the outer wall are same as that of the ambient air as evident from figures 5 (a) and 5 (b). But the situation changes when preheated air is used. Higher isotherms are noted even near the wall as shown in Fig. 5 (c) and Fig. 5 (d) without and with considering radiation respectively. Also when radiation is considered, more uniform temperature distribution is obtained with preheated air.

### 3.3. Soot Volume Fraction Distribution

Soot volume fraction, soot number density and soot diameter are three important parameters used to describe the distribution and morphology of soot in a flame.

The soot volume fraction isopleths for the four flames considered for the study have been shown in figures 6 (a) to 6 (d). The values of different isopleths are also shown in each figure. From the figures, it is observed that the distribution patterns are somewhat same for all the cases, but the amounts of soot formed are different in different flames. Major portions of the soot have been accumulated within a particular zone of the combustor as are evident from the distribution contours with the soot volume increasing in the inward direction of the closed contours.

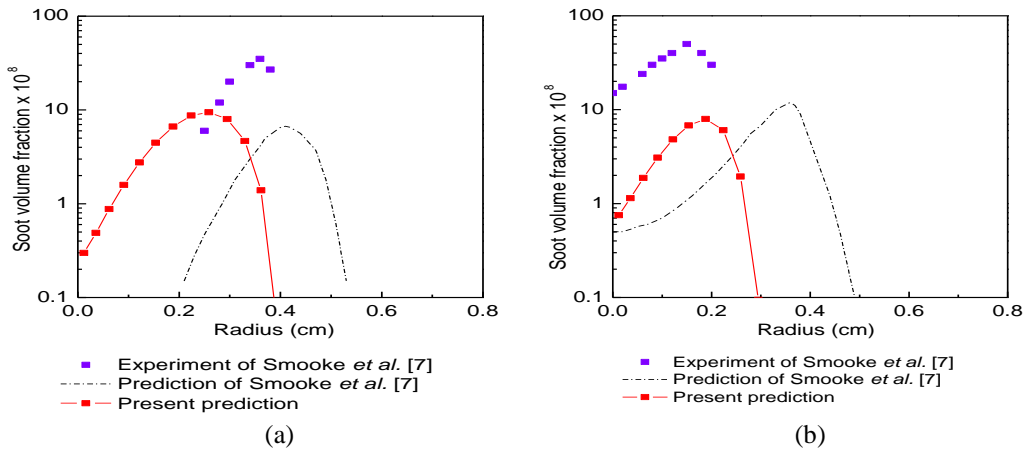


Figure 4. Comparison of soot volume fraction at non-dimensional heights (a) 0.50 and (b) 0.70 for the base flame.

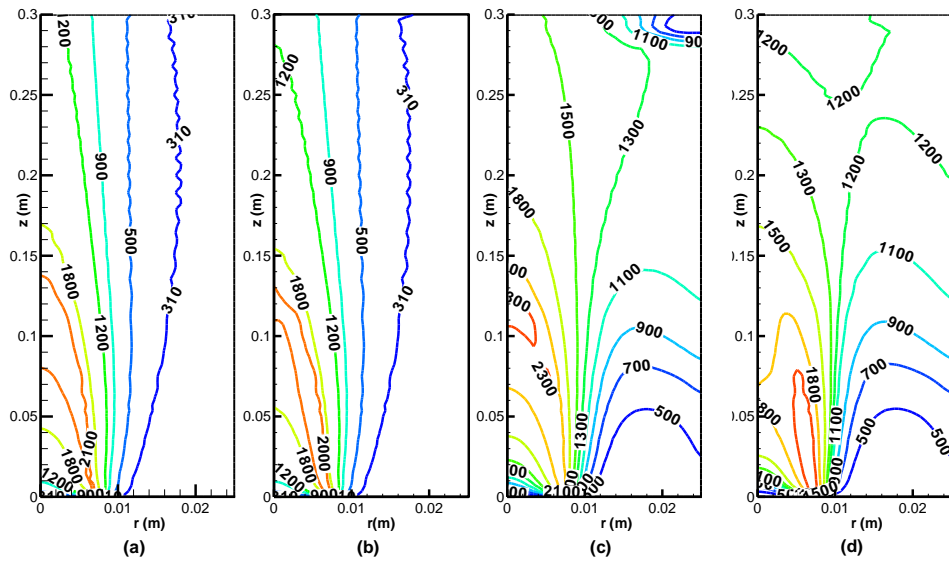


Figure 5. Temperature (in K) contours: (a) Flame I (WR 300), (b) Flame II (R 300), (c) Flame III (WR 400) and (d) Flame IV (R 400).

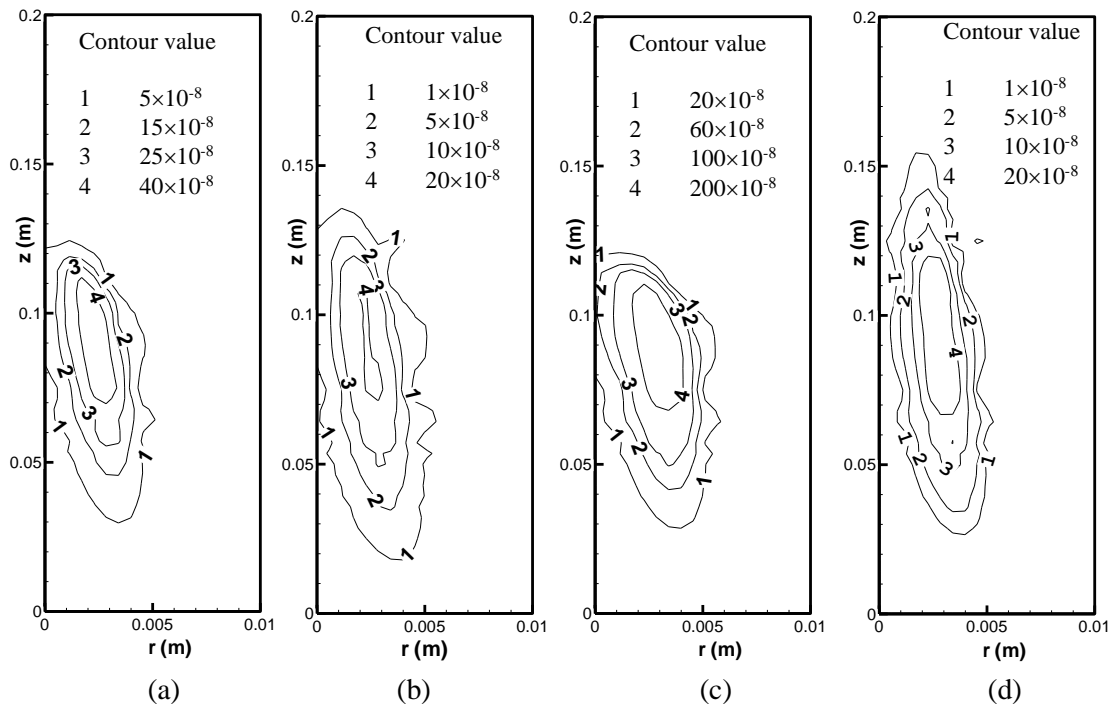


Figure 6. Soot volume fraction isopleths for: (a) Flame I (WR 300), (b) Flame II (R 300), (c) Flame III (WR 400) and (d) Flame IV (R 400).

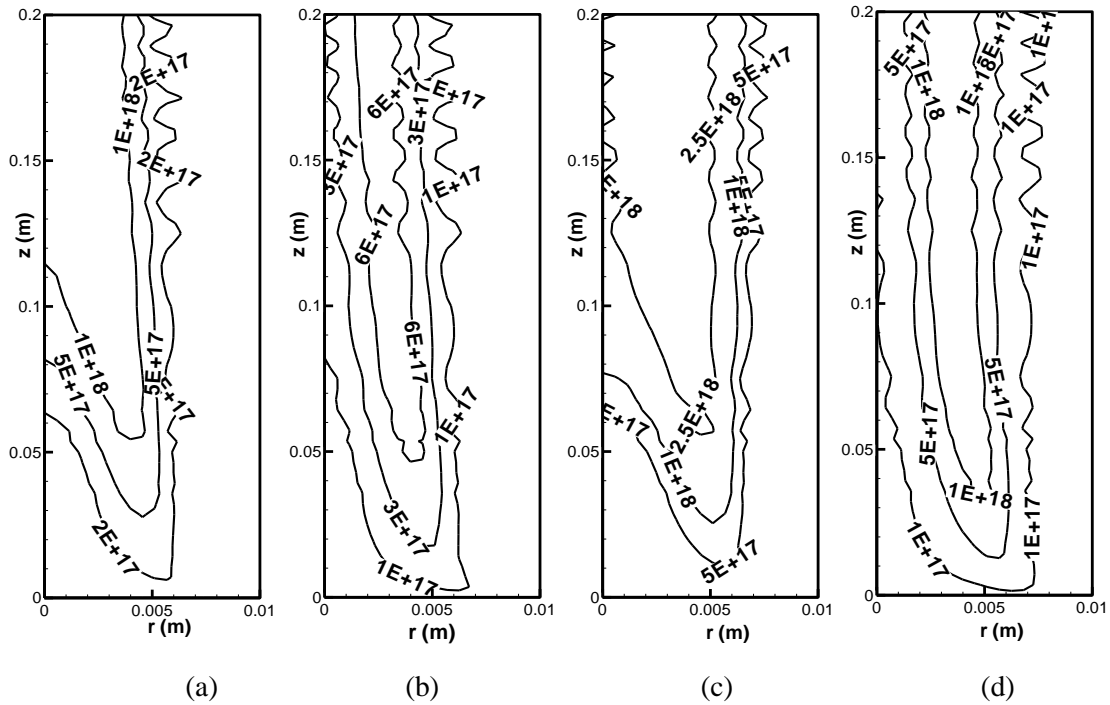


Figure 7. Soot number density contours for: (a) Flame I (WR 300), (b) Flame II (R 300), (c) Flame III (WR 400) and (d) Flame IV (R 400).

A close look of the patterns of figures 6 (a) and 6 (c) reveals that when radiation is not considered, comparatively more soot is observed for both the non-preheating and preheating conditions. It is also clear from the figures that the soot volume increases with the preheating. A soot volume fraction contour of  $40 \times 10^{-8}$  is noted to be persisting in the central part of the soot containing zone in case of non-preheated air and this value becomes as high as  $200 \times 10^{-8}$  with preheated air.

When radiation is considered, the oval shaped contours are observed for both non-preheating and preheating cases. But the corresponding soot volume fraction value decreases by a factor of 2 for non-preheated case (flame II) and by a factor of almost 3 for preheated case (flame IV). In these cases, the soot volume also increases with preheating as evident from figures 6 (b) and 6 (d). From the comparison of the figures 6 (a) and 6 (b), and 6 (c) and 6 (d), it is clearly observed that radiation affects the amount of soot volume whether the air is preheated or not. The soot volume reduces for both non-preheated and preheated air considering the radiation, and the reduction is more in case of preheated air. It may be noted that the soot is much lower along the centerline (i.e. axis of the geometry considered) in all four flame conditions. From figure 4, it is also observed that soot volume fraction is negligible beyond a certain axial heights in all the cases. This is due to the soot surface oxidation.

### 3.4. Soot Number Density

The distributions of soot number density as a functions of radial and axial co-ordinates have been shown for four flames in figures 7 (a) to 7 (d) respectively. It is observed from figures 7 (a) and 7(c) that, the patterns of contours are similar for non-preheated and preheated air neglecting the radiation effects. However, the number density increases by a factor of almost 2.5 in case of preheated air. Also, soot containing zone having appreciable amount of soot particle, elongates in the radial direction with the preheated air. This is caused due to more uniform temperature distribution in

case of preheated air (Fig. 5). Radiation heat loss does not change the distribution pattern, but lowers the soot number density. Soot inception or soot nucleation is very much temperature dependent and radiation heat loss from the soot as well as from the gas band decreases the temperature resulting in lower soot particle density throughout the computation zone as observed in figures 7 (b) and 7 (d). For all four flame conditions, except at lower height, the contour lines are almost vertical and extend beyond the computational domain in the axial direction. The presence of soot particle through the axial height suggests that only small size soot particles are present even above an axial height 0.15 m and some of them escape the computational zone also. The contribution from these towards the soot volume fraction is negligible.

### 3.5. Soot Diameter Distribution

The soot particle size in term of mean diameter is calculated from soot volume fraction and soot number density assuming the particles to be spherical from the following equation:

$$f_v = \frac{\pi}{6} n d_s^3 \quad (21)$$

The contours of different soot diameters for different flames have been presented in figures 7 (a) to 7 (d). From the figures, it is clear that the distribution patterns are almost same in the radial direction for all the cases except flame IV. In the first three cases, lowest soot particle size of 2 nm diameter is available upto an axial height of 0.12 to 0.13 m only, whereas in case of the fourth flame (with preheating and radiating conditions), it extends beyond 0.2 m axial height also. From the figures, it can also be stated that the changes in magnitudes of soot diameters are negligible due to radiation, but soot diameters increase from 8 nm to 11 nm with preheating of the inlet air.

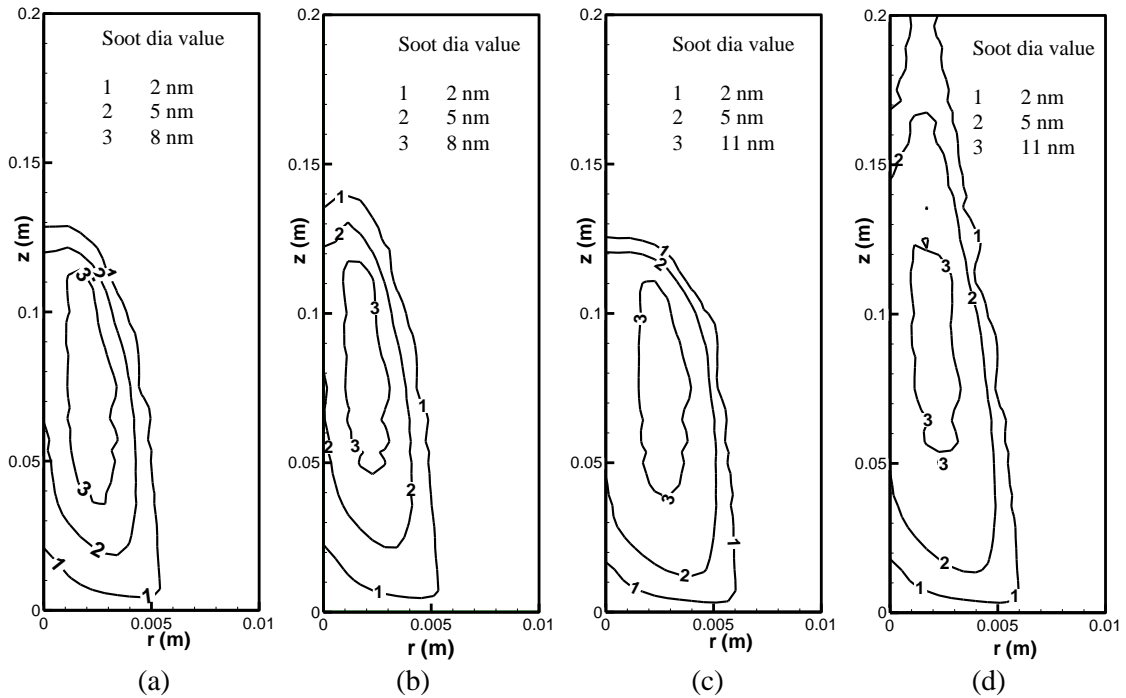


Figure 8. Soot diameter contours for: (a) Flame I (WR 300), (b) Flame II (R 300), (c) Flame III (WR 400) and (d) Flame IV (R 400).

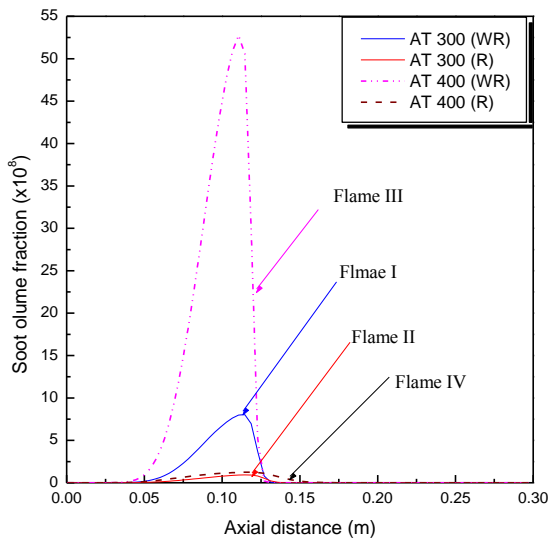


Figure 9. Centre line soot volume distribution for: (a) Flame I (WR 300), (b) Flame II (R 300), (c) Flame III (WR 400) and (d) Flame IV (R 400).

volume fraction profiles are almost same for non-preheated and preheated air. From the plot, it is clearly observed that within a small axial length, soot volume increases rapidly, reaches to a maximum value and then decreases rapidly for both non-preheated and preheated air. But, the maximum value of soot volume fraction is much higher (around  $52 \times 10^{-8}$ ) than that of non-preheated air (around  $8 \times 10^{-8}$ ). It is also noted that the peak point is slightly shifted towards the upper direction of the burner compared with the case of preheated air. When radiation is considered, the soot volume fraction decreases significantly and the distribution is almost flat in the soot containing zone for both non-preheated and preheated air. As the temperature is lowered due to radiation, there is a sharp fall in soot volume. From the figure, it is evident that the maximum drop in soot occurs between the flame II and Flame III. Clearly, both radiation and air-preheating have prominent effect on centerline soot formation.

Table 2. Comparison of Total Soot Volume, Soot Number and Soot Yield for Different Flame Conditions.

Flame Identification	Flame conditions	Total soot vol. fraction ( $\text{m}^3/\text{s}$ )	Total soot number (/s)	Soot yield (%)	Remarks
Flame I	AT 300 (WR)	$1.08353 \times 10^{-12}$	$2.32637 \times 10^{-13}$	0.07009	-
Flame II	AT 300 (R)	$0.50339 \times 10^{-12}$	$1.20783 \times 10^{-13}$	0.03256	Lowest
Flame III	AT 400 (WR)	$7.60740 \times 10^{-12}$	$9.37934 \times 10^{-13}$	0.49212	Highest
Flame IV	AT 400 (R)	$2.82073 \times 10^{-12}$	$3.43033 \times 10^{-13}$	0.18247	-

### 3.6. Centerline Soot Volume Fraction

The centerline soot volume fraction profiles for the four flames considered here, have been plotted in figure 9. In the legend of the figure, AT denotes air inlet temperature, WR denotes the case of neglecting radiation effect, R indicates the case where radiation has been taken into consideration. When radiation is not considered, nature of the soot

### 3.7. Soot Yield

Although soot is primarily confined to a small zone within and around the flame, mass of the total soot is estimated for the whole computational zone to define a term called soot yield. The soot yield is defined as the ratio of mass of the total soot formed and the mass of carbon supplied through the hydrocarbon fuel (methane) on unit

time basis [23]. Mathematically, it can be written on percentage basis as

$$Y_s = \frac{\int 2\pi r v \rho_s f_v dr}{m_c} \times 100 \quad (22)$$

where  $v$  is the velocity,  $\rho_s$  is the density of soot,  $f_v$  is the soot volume fraction and  $m_c$  is the mass of carbon in the fuel. The calculated values of total soot, soot number and soot yield for four flames considered in this work have been presented in table 2. When radiation is not considered, total soot formed and soot yield using preheated air is approximately 7 times than that with non-preheated air. Total soot number also increases with preheating, but it is about four times only. It indicates that soot surface growth enhances more rapidly than soot nucleation with preheating. If the radiation heat loss is considered, the above factor decreases to 5.60 and 2.84 respectively. If we compare the radiation effect only separately for non-preheated and preheated air, it is observed that the effect is more in case of preheated air than non-preheated air. Total soot formed and the soot yield decrease by a factor of about 2.1 and the soot number decreases by a factor of 1.9 due to radiation in case of non-preheated air. The corresponding values are noted to be approximately 2.69 and 2.73 respectively for preheated air. Probably this happens due to decrease in temperature for radiation heat loss from the gas mixture and soot. As the activation temperature for soot nucleation is higher than that of soot surface growth, the soot surface growth increases more rapidly than the nucleation rate with the increase in temperature due to the use of preheated air.

#### 4. Conclusions

In the present study the effects of radiation heat loss and preheating of air on the temperature distribution and formation of soot have been analyzed numerically in a confined laminar diffusion flame of methane and air. The numerical simulation has been carried out with the help of in-house developed code in FORTRAN. When radiation is considered the maximum temperature is reduced by around 100 K for non-preheated case and this reduction is even more with preheated air. A reduction in soot volume fraction is observed considering the radiation for both the non-preheated and preheated flames, but soot volume fraction is found to be more with preheating for radiative as well as non-radiative cases. When radiation is considered, the soot volume fraction values have been noted to reduce by a factor of 2 for non-preheated case and by a factor of almost 3 for preheated case. It is also noted that the soot is much lower along the centerline for all the considered cases. The soot number density increases by a factor of almost 2.5 in case of preheated air. Radiation heat loss does not change the distribution pattern, but lowers the soot number density. No appreciable change in soot diameter is observed due to radiation but soot diameter increases with the use of preheated air. Soot yield decreases due to radiation heat loss both in case of non-preheated and preheated air. Use of preheated air increases the soot yield for both the radiative and non-radiative flames.

#### Nomenclature

$C_j$	Concentration of $j$ th species
$C_p$	Specific heat
$d_s$	Soot particle diameter

$f_v$	Soot volume fraction
$g$	Acceleration due to gravity
$h$	Enthalpy
$L_e$	Lewis number
$N_o$	Avogadro number
$n$	Soot particle number density
$p$	Pressure
$r$	Radial distance
$T$	Temperature
$t$	Time
$v$	Velocity
$z$	Axial distance

#### Greek Symbols

$\mu$	Viscosity
$\rho$	Density
$\lambda$	Thermal conductivity
$\sigma$	Stefan-Boltzmann constant
$\phi$	General variable in conservation equation

#### Subscripts

$a$	Air
$f$	Fuel species
$j$	Species identification
$r$	Radial direction
$z$	Axial direction
$s$	Soot

#### References

- [1] Ku, J. C., Tong, U., and Greenberg P. S. Measurements and modeling of soot formation and radiation in microgravity jet diffusion flames. HTD-Vol. 335, Proc. of the ASME Heat Transfer Division, Vol. 4, ASME 1996.
- [2] McEnally, C. S., Schaffer, A. M., Long, M. B., Pfefferle, L. D., Smooke, M. D. and Colket, M. B. Computational and experimental study of soot formation in a coflow laminar ethylene diffusion flame. Twenty-Seventh Symposium (International) on Combustion, The Combustion Institute, 1497-1505, 1998.
- [3] Syed, K. J., Stewart, C. D. and Moss, J. B., Modeling soot formation and thermal radiation in buoyant turbulent diffusion flames. Twenty Third Symposium (International) on Combustion, The Combustion Institute, 1533-1541, 1990.
- [4] Moss, J. B., Stewart, C. D. and Young, K. J. Modeling soot formation and burnout in a high temperature laminar diffusion flame burning under oxygen-enriched conditions. *Combustion Flame*, 101, 491-500, 1995.
- [5] Said, R., Garo, A. and Borghi, R. Soot formation modeling for turbulent flames. *Combustion Flame*, 108, 71-86, 1997.
- [6] Sivathanu, Y. R. and Gore, J. P. Effects of gas-band radiation on soot kinetics in laminar methane/air diffusion flames. *Combustion Flame*, 110, 256-263, 1997.
- [7] Smooke, M. D., McEnally, C. S., Pfefferle, L. D., Hall, R. J. and Colket, M. B. Computational and experimental study of soot formation in a coflow laminar diffusion flame. *Combustion Flame*, 117, 117-139, 1999.

- [8] Liu, F., Guo, H., Smallwood, G. J. and Gulder, Omer L. Effects of gas and soot radiation on soot formation in a coflow laminar ethylene diffusion flame. *J. Quantitative Spectroscopy & Radiative Transfer*, 73, 409-421, 2002.
- [9] Guo, H., Liu, F., Smallwood, G. J. and Gulder, Omer L. The flame preheating effect on numerical modeling of soot formation in a two-dimensional laminar ethylene-air diffusion flame. *Combustion Theory and Modeling*, 6, 173-187, 2002.
- [10] Smooke, M. D., Long, M. B., Connelly, B. C., Colket, M. B. and Hall, R. J. Soot formation in laminar diffusion flames. *Combustion Flame*, 143, 613-628, 2005.
- [11] Kamal, M. M. Soot formation and oxidation in normal and inverse diffusion flames. *J. Power Energy*, 221, 481-495, 2007.
- [12] Saji, C. B., Balaji, C. and Sundarajan, T. Investigation of soot transport and radiative heat transfer in an ethylene jet diffusion flame. *Int. J. Heat Mass Transfer*, 51, 4287-4299, 2008.
- [13] Mitchell, R. E., Sarofim, A. F., and Clomburg, L. A. Experimental and numerical investigation of confined laminar diffusion flames. *Combustion Flame*, 37, 227 – 244, 1980.
- [14] Smooke, M. D., Mitchell, R. E. and Keys, D. E. Numerical solution of two-dimensional axisymmetric laminar diffusion flames. *Combustion Sci. Technology*, 67, 85-122, 1989.
- [15] Datta, A. and Saha, A., Contributions of self-absorption and soot on radiation heat transfer in a laminar methane-air diffusion flame. *Proc. of IMechE.*, 221, 955-970, 2006.
- [16] Barlow, R. S., Karpetis, A. N., Frank, J. H. and Chen, J. Y. Scalar profiles and NO-formation in laminar opposed flow partially premixed methane/air flames. *Combustion Flame*, 127, 2102-2118, 2001.
- [17] Lee, K. B., Thring, M. W. and Beer, J. M. On the rate of soot in a laminar soot flame. *Combustion Flame*, 6, 137-145, 1962.
- [18] Santoro, R. J., Yeh, T. T., Horvath, J. J., and Semerjian, H. G. The transport and growth of soot particle in laminar diffusion flames. *Combustion Sci. Technol.*, 53, 89-115, 1987.
- [19] Hirt, C. W., and Cook, J. L. Calculating three-dimensional flows around structures and over rough terrain. *J. Comp. Phys.*, 10, 324–338, 1972.
- [20] Datta, A. Effects of variable property formulation on the prediction of a CH<sub>4</sub>-air laminar jet diffusion flame. Proc. of the ISHMT/ASME Heat and Mass Transfer Conference, Tata McGraw-Hill, India, 532, 2004.
- [21] Patankar, S. V., Numerical heat and mass transfer and fluid flow, Hemisphere, New York, 1980.
- [22] Hirt, C. W., Nickols, B. D., and Romero, N. C. SOLA – A Numerical Solution Algorithm for Transient Fluid Flows. Los Alamos Scientific Laboratory Report, LA – 5852, Los Alamos, New Mexico, 1975.
- [23] Guo, H., Trottier, S., Johnson, M. R. and Small wood, G. J., A numerical investigation on soot formation from laminar diffusion flames of ethylene/methane mixture. Proc. of Summer Heat Transfer Conference, USA, 1-7, 2008.